Draft version August 5, 2014
Preprint typeset using LaTeX style emulateapj v. 12/16/11

arXiv:1407.8260v2 [astro-ph.SR] 4 Aug 2014

SUPERNOVA REMNANT W49B AND ITS ENVIRONMENT

H. Zhu[1], W. W. Tian[1,2], P. Zuo[1]
[1]Key Laboratory of Optical Astronomy, National Astronomical Observatories, Chinese Academy of Sciences, Beijing 100012, China; zhuhui@bao.ac.cn and tww@bao.ac.cn and
[2]Department of Physics & Astronomy, University of Calgary, Calgary, Alberta T2N 1N4, Canada
Draft version August 5, 2014

ABSTRACT

We study Gamma-ray supernova remnant W49B and its environment using recent radio and infrared data. *Spitzer* IRS low resolution data of W49B shows shocked excitation lines of H_2 (0,0) S(0)-S(7) from the SNR-molecular cloud interaction. The H_2 gas is composed of two components with temperature of ∼260 K and ∼1060 K respectively. Various spectral lines from atomic and ionic particles are detected towards W49B. We suggest the ionic phase has an electron density of ∼500 cm^{-3} and a temperature of ∼10^4 K by the spectral line diagnoses. The mid- and far-infrared data from *MSX*, *Spitzer* and *Herschel* reveals a 151 ± 20 K hot dust component with a mass of 7.5 ± 6.6 × $10^{-4} M_\odot$ and a 45 ± 4 K warm dust component with a mass of 6.4 ± 3.2 $M_\odot$. The hot dust is likely from materials swept up by the shock of W49B. The warm dust may possibly originate from the evaporation of clouds interacting with W49B. We build the HI absorption spectra of W49B and nearby four HII regions (W49A, G42.90+0.58, G42.43-0.26 and G43.19-0.53), and study the relation between W49B and the surrounding molecular clouds by employing the 2.12 μm infrared and CO data. We therefore obtain a kinematic distance of ∼10 kpc for W49B and suggest that the remnant is likely associated with the CO cloud at about 40 km s^{-1}.

Subject headings: ISM: supernova remnants — ISM: individual (W49B) — radio lines: ISM — submilimeter: ISM — cosmic rays

1. INTRODUCTION

Massive stars ($\geq 8M_\odot$) evolve quickly. After they end with core-collapse supernova explosion and form supernova remnants (SNRs), their mother molecular clouds should be still nearby. It is expected that the mother clouds will shape the SNRs significantly and SNRs also remold the surrounding medium, e.g. ejecting newly formed dust to the medium, changing the ingredient of dust swept up by the shock, triggering molecule cloud core collapse and producing cosmic rays.

W49B is a mixed-morphology (MM) SNR and one of the brightest sources in the Galaxy at 1 GHz (Keohane et al. 2007, Moffett & Reynolds 1994). Multifrequency radio observations of W49B show a 4′ box or barrel like structure with amount of distorted filaments. W49B has an integrated spectral index of about -0.48. Polarization is detected at 6 cm but with very low mean polarized fraction of 0.44% ± 0.06%. Moffett & Reynolds (1994) explained the low fraction as depolarization caused by tangled magnetic fields on the shell or Faraday depolarization within the remnant. The 1.64 μm [Fe II] image reveals similar barrel like structure as the radio displayed. The shocked molecular hydrogens traced by the H_2 (1,0) S(1) line at 2.12 μm are found nearly surrounding W49B with strong emission at the east, south and west boundaries. Keohane et al. (2007) suggested these as evidences of W49B born in a wind-blown bubble inside a dense molecular cloud.

Early X-ray observations carried out by *Einstein*, *EXOSAT* and *ASCA* (Pye et al. 1984; Smith et al. 1985; Fujimoto et al. 1995; Hwang et al. 2000) show the X-ray emission is thermal and ejecta dominated. Based on these features, the age of W49B is estimated from 1000 yr to 4000 yr. *ASCA* observation discloses that the Fe emissions trend to rise in the inner part of the SNR while the emission of Si, S extents to the outer region. It also provides evidence of overabundances of Si, S, Ar, Ca and Fe through fitting the global spectrum. Thanks to the high spacial resolution and sensitivity of *XMM-Newton*, *Chandra* and *Suzaku*, more striking secrets about W49B were exposed (Miceli et al. 2006, 2010, Lopez et al. 2009, 2013a,b, Ozawa et al. 2009, Yang et al. 2013). First, W49B has the most elliptical and elongated morphology in young, X-ray bright SNRs. Second, elemental segregation is confirmed with the Si, S, Ar, Ca showing more extended homogeneous structure but the iron nearly missing from the west. Third, silicon burning products, Cr and Mn, are detected in W49B's spectrum. Finally, W49B shows clear overionization feature which may be caused by rapid cooling. Other SNRs with overionized plasmas usually have ages older than ∼4000 yr. Since W49B is young, this indicates that overionization can occur in the SNR's early evolution stage.

GeV and TeV γ-rays have been detected just coincident with the radio brightest part of W49B (Abdo et al. 2010, Brun et al. 2011). The observed γ-ray photon spectrum is very steep. Its spectral index is at least 0.5 higher than the electron spectral index. This favors a hadronic origin for the γ-ray radiation (Mandelartz & Becker Tjus 2013). Other evidences supporting the hadronic model include: (1) the observed high GeV γ-ray luminosity and (2) dense molecular

clouds interacting with W49B (Brun et al. 2011). More detail information about the ambient of W49B is needed for further study of the γ-ray emission.

To explain the characters of W49B, two scenarios are proposed: one is a jet driven bipolar explosion of a massive star, another is a normal spherical supernova exploded in inhomogeneous medium. Currently there are more evidences supporting the first model (Lopez et al. 2013a): (1) near infrared and radio images show a barrel like morphology which is common in bubble blown by massive star; (2) X-ray data reveals the jet like elongated structure; (3) the abundance of Si, S, Ar and Ca (relative to Fe) favors an aspherical explosion by a 25 $M_{\odot}$ progenitor; (4) no neutron star or pulsar is detected in W49B. The normal spherical supernova model can explain most of the observed traits. However, this model is not able to produce the observed element abundance and the ejecta mass is also too big to be explained easily (Miceli et al. 2010). Therefore the picture that W49B originates from a jet driven bipolar explosion of a 25 $M_{\odot}$ massive star with its morphology shaped by the interstellar medium is more favorite. But how the environment effects the morphology of W49B is still little known (Zhou et al. 2011).

Distance is another confusion for W49B. HI absorption spectra toward W49B and its nearby HII region W49A which has a distance of 11.4 kpc (Gwinn, Moran, & Reid 1992) have been given by Radhakrishnan et al. (1972), Lockhart & Goss (1978) and Brogan & Troland (2001). Compared with W49A, W49B is lack of HI absorption at velocities of $\sim$10 km s^{-1} and $\sim$55 km s^{-1}. The absence of absorption at 55km s^{-1} hints W49B is $\sim$3 kpc closer than W49A (Radhakrishnan et al. 1972). Brogan & Troland (2001) found the N_{HI}/T_s image toward W49A and W49B have obvious change on size scales of about $1'$. They thought the differences in the absorption spectra of W49A and W49B could be explained without assuming W49B is closer, but with scenarios involving differences on kinematics, distribution and temperature. They suggested W49B might have the same distance as W49A based on the possible interaction between the SNR and the HI cloud at $\sim$5 km s^{-1}. Recently, Chen et al. (2014) noticed that CO($J = 2-1$) emission map at 39-40 km s^{-1} for W49B show possible cavity structure, but no robust kinematic evidence has been obtained yet. The authors suggested if this SNR-molecular cloud association is true, the kinematic distance to W49B is 9.3 kpc.

To understand W49B and its environment better, we perform a radio and infrared study toward this SNR. In section 2, we give a description about the data. The results are presented in section 3. A discussion about the properties of W49B and its environment, such as the distance, shock and dust, is in section 4. Section 5 is a summary.

2. DATA AND DATA REDUCTION

2.1. *Radio data*

The 1420 MHz radio continuum and HI emission data come from the Very Large Array Galactic Plane Survey (VGPS, Stil et al. 2006). The continuum data has a spatial resolution of $1'$ and a noise of 0.3 K. The HI spectral line images have a resolution of $1' \times 1' \times$ 1.56 km s^{-1} and an noise of 2 K per channel. We also use the 20 cm continuum data from the Multi-Array Galactic Plane Imaging Survey which have resolution of $\sim 6''$ (MAGPIS, Helfand et al. 2006). The ^{13}CO($J = 1-0$) spectral line data is from the BU-FCRAO Galactic Ring Survey (Jackson et al. 2006). The data has an angular and spectral resolution of $46''$ and 0.21 km s^{-1} with noise of about 0.13 K, respectively. We get the CO($J = 3-2$) data from the first release of *JCMT* CO High-Resolution Survey (Dempsey, Thomas, & Currie 2013). The data is smoothed to a velocity resolution of 1 km s^{-1} and a spatial resolution of $16.6''$. The noise in the region of W49B is about 0.44 K.

2.2. *Infrared data*

The *Spitzer* Infrared Spectrograph (IRS, Houck et al. 2004) observation of W49B is taken on 24 April 2005 using the staring mode (Program ID: 3483, PI: Rho, J.). The short-low slit (SL, 5.2-14.5 μm) and long-low slit (LL, 14.0-38.0 μm) are used in the observation. The bad and rogue pixels of the co-added BCD frames are corrected with the IRSCLEAN tool provided by the Spitzer Science Center. Since W49B is extended, only different orders are used to remove the unrelated diffuse emission in the direction of the SNR. After background subtraction, an optimal spectrum is extracted by the SPICE software. The spectrum extraction region is selected to meet criterion of the brightest overlapped region between SL and LL. Error in the final extraction is of the order of 10% which are mainly caused by the background subtraction (Andersen et al. 2011).

The *Herschel* observation are taken on 24 October 2010 as part of the *Herschel* Infrared Galactic Plane Survey (Hi-GAL). The PACS (Poglitsch et al. 2010) and SPIRE (Griffin et al. 2009) are used under the parallel mode. The covered bands are 70 μm, 160μm, 250 μm, 350 μm and 500 μm. Each bands have a measured beam of $\sim 9.7'' \times \sim 10.7''$, $\sim 13.2'' \times \sim 13.9''$, $\sim 22.8'' \times \sim 23.9''$, $\sim 29.3'' \times \sim 31.3''$ and $\sim 41.1'' \times \sim 43.8''$ respectively (Traficante et al. 2011). The PACS bands (70 μm and 160 μm) have been processed using the standard pipeline. Since the SPIRE data has a problem of stripe, we re-process them by combining the scripts 'Photometer Map Merging' with 'Baseline Removal and Destriper' to merge the two direction scan data to a single map. We also remove the SPIRE observation baseline and do a correction for the relative gain of bolometer. The process uses scripts within the software package *Herschel* Interactive Processing Environment (HIPE, version 11.0.1) and calibration tree 11.0, which was the most up-to-date version at the time.

The 2.12 μm data is from 'UKIRT Widefield Infrared Survey' for H_2 (Froebrich et al. 2011). Other infrared continuum image of *WISE* 12 μm (Wright et al. 2010), *Spitzer* 24 μm (Carey et al. 2009), *MSX* 12.1 μm, 14.7

μm and 21.3 μm (Price et al. 2001) are collected directly from NASA/IPAC Infrared Science Archive.

3. RESULTS

3.1. HI *absorption spectra*

The left panel of Figure 1 displays the 1420 MHz continuum image around W49B. We build the HI absorption spectrum by the revised methods presented by Tian et al. (2007) and Tian & Leahy (2008). The methods minimize the possibility of a false absorption spectrum due to the potential HI distribution difference in two lines of sight. In the right panel, the marked white boxes are used to extract the spectra. Regions between the white boxes and yellow boxes are the background. For W49B, we select two bright regions to analyze its HI absorption spectrum.

Figure 2 shows the HI absorption spectra of W49B, W49A and three nearby HII regions. The ^{13}CO($J = 1 - 0$) spectral lines in each panel are extracted from the same regions as HI spectra. There are three main HI absorption features in the spectra which are at ∼10 km s^{-1}, the ∼40 km s^{-1} and the ∼60 km s^{-1} respectively. For HII regions G42.43-0.26 and G43.19-0.53, radio recombination lines are detected at 62.7 km s^{-1} and 55.0 km s^{-1} (Lockman 1989). Since HI absorptions appear up to ∼70 km s^{-1}, the two HII regions are located at the far side distances, i.e. ∼7.8 kpc and ∼8.4 kpc respectively (using the Galactic rotation curve model with $R_\odot = 8.5$ kpc and $V_\odot = 220$ km s^{-1}). Therefore the ∼10 km s^{-1} absorption of G42.43-0.26 and G43.19-0.53 likely originates from local HI clouds. HII region G42.90+0.58 (Wood & Churchwell 1989) is located outside the solar circle because of its absorption at negative velocity. The trigonometric parallax measurement (Gwinn, Moran, & Reid 1992) gives W49A a distance of 11.4 kpc which is consistent with the far side kinematic distance of ∼10 km s^{-1}. Compared with the absorption spectra of G42.43-0.26 and G43.19-0.53, stronger absorption at ∼10 km s^{-1} is detected towards both W49A and G42.90+0.58. This is because the absorption at 10 km s^{-1} of W49A and G42.90+0.58 arises from both local and Perseus spiral arm.

The absorption spectrum of W49B displays similar features as G42.43-0.26 and G43.19-0.53 at the ∼10 km s^{-1} and no absorption at ∼12 km s^{-1} (also see the HI channel map in Figure 3), so reasonably its absorption at 10 km s^{-1} likely originates from the local HI gas. The lack of absorption from Perseus spiral arm hints its distance is likely closer than W49A. To confirm this, we calculate the optical depth assuming W49B is located at the same distance as or behind W49A, i.e. 11.4 kpc. The brightness temperature of HI emission at velocity of ∼12 km s^{-1} in the direction of W49B is T_b = 70 - 80 K. Assuming the background continuum emission is very low (T_{bg} = 0 K) and the spin temperature of HI cloud (T_s) ranges from 90 to 300 K. The Radiative transfer equation gives the HI optical depth $\tau_{HI} = -\ln(1 - \frac{T_b}{T_s})$, so we derive a τ_{HI} of 0.3 - 2.2 which is above the detection sensitivity of 0.1. Since no absorption at ∼12 km s^{-1} is detected, W49B should be closer than W49A. Further analysis will be presented in the discussion section.

TABLE 1
SURFACE BRIGHTNESS OF EMISSION LINES OF W49B

Transition	λ μm	Observed Brightness erg cm^{-2} s^{-1} sr^{-1}	De-reddened Brightness erg cm^{-2} s^{-1} sr^{-1}
H_2 S(7)	5.51	7.56(0.92)E-4	1.22(0.14)E-3
H_2 S(6)	6.11	2.99(0.42)E-4	4.74(0.63)E-4
H_2 S(5)	6.91	1.14(0.13)E-3	1.64(0.19)E-3
H_2 S(4)	8.03	3.85(0.49)E-4	7.71(0.93)E-3
H_2 S(3)	9.67	2.35(0.28)E-4	1.59(0.18)E-3
H_2 S(2)	12.28	1.82(0.22)E-3	3.83(0.43)E-4
H_2 S(1)	17.04	4.88(0.64)E-5	9.35(1.17)E-5
H_2 S(0)	28.22	1.05(0.45)E-5	1.55(0.65)E-5
[Fe II]	5.34	5.89(0.78)E-4	9.76(1.24)E-4
[Ar II]	6.98	3.37(0.56)E-4	4.85(0.77)E-4
[Ne II]	12.8	7.95(0.85)E-4	1.48(0.16)E-3
[Cl II]	14.37	1.63(0.34)E-5	2.48(0.49)E-5
[Ne III]	15.5	2.93(0.31)E-4	4.94(0.52)E-4
[Fe II]	17.9	1.22(0.14)E-4	2.45(0.27)E-4
[S III]	18.7	4.97(0.65)E-5	1.00(0.12)E-4
[Fe II]	24.5	4.10(0.54)E-5	5.57(0.73)E-5
[S I]	25.2	4.12(0.55)E-5	6.50(0.84)E-5
[Fe II]	25.9	3.16(0.34)E-4	4.78(0.50)E-4
[S III]	33.5	4.80(0.71)E-5	6.96(0.98)E-5
[Si II]	34.8	1.13(0.11)E-3	1.51(0.16)E-3
[Fe II]	35.35	2.77(0.84)E-4	3.75(1.14)E-4

3.2. *Spitzer IRS low resolution spectrum*

Figure 4 shows the IRS map of W49B. Short boxes represent the SL slits and the long boxes are for the LL slits. To correct the extinction, we use the dust model of Draine (2003) with $R_V = 3.1$. The selected hydrogen column density of 4.8×10^{22} cm^{-2} is the average of several X-ray observations' results (e.g. Hwang et al. 2000, Miceli et al. 2006, Keohane et al. 2007). The final spectrum is presented in Figure 5.

We calculate the flux of each spectral line through a gauss fitting before and after extinction correction. The results are listed in Table 1. As displayed in Figure 5 and Table 1, pure rotational transition lines of H_2 (0,0) S(0)-S(7) are detected. Since these bright lines usually appear in the shocked region, this supports that W49B is interacting with molecular clouds at its southwest boundary. Beside the molecular lines, forbidden transition lines of atom and ions are also detected, i.e. lines from S^0, S^{2+}, Ar^+, Cl^+, Fe^+, Ne^+, Ne^{2+} and Si^+. Detecting spectral lines from different gas phase suggests W49B has a complex environment.

3.3. *Dust revealed by multi-infrared image*

Figure 6 presents the middle and far infrared images (from the *WISE*, *Spitzer* and *Herschel*) and the 20 cm continuum image from MAGPIS. W49B's morphology in the infrared images with wavelength less or equal to 70 μm is similar with that in the radio image which indicates that the infrared emissions are correlated with W49B. At 160 μm, unrelated foreground and background cold dust emissions begin to dominate the image, but weak features correlating with the radio

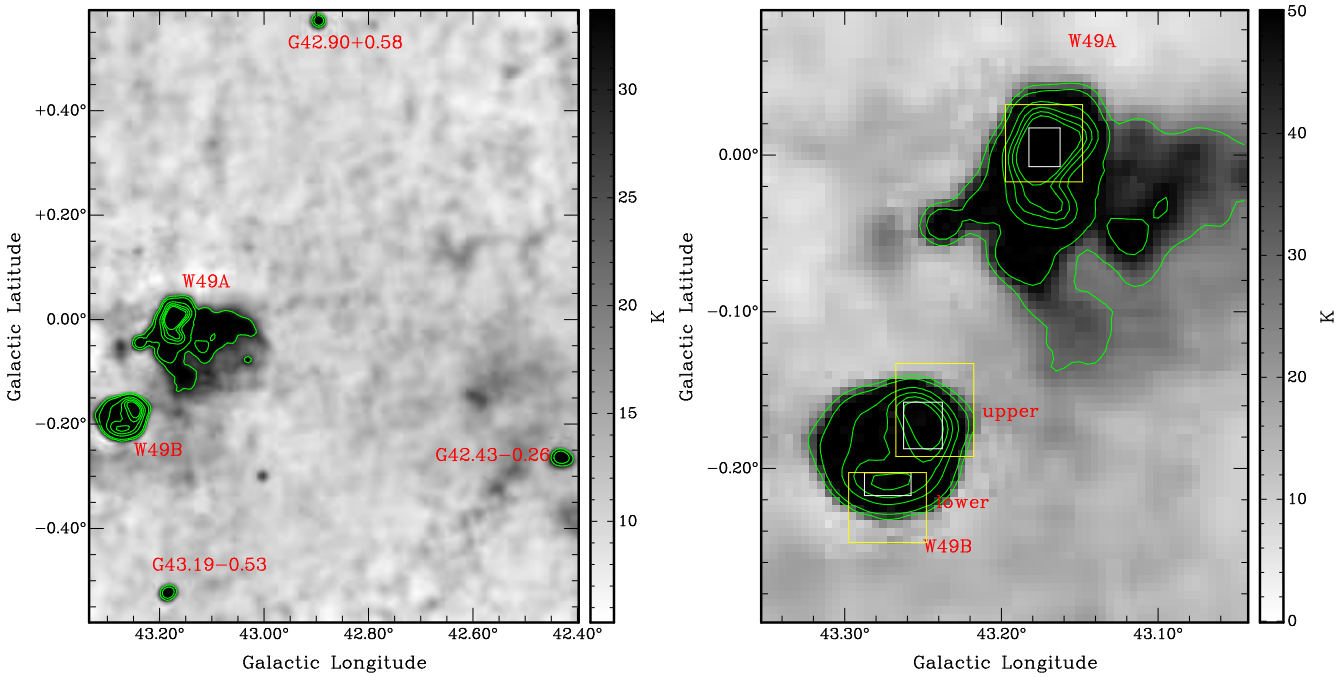

FIG. 1.— Left: The VGPS 1420 MHz continuum image around W49B with contour levels of 30, 50, 150, 250, 350 and 450 K. Right: White boxes are the source-on regions to extract the absorption spectra, and the regions between white and yellow boxes are used to subtract the background.

emission can still be seen. For longer wavelengths, infrared emissions related with W49B entirely disappear in the images.

We fit the spectral energy distribution (SED) to understand the property of dusts related with W49B. In the Figure 6c, we select the region within the polygon excluding the circle to extract the emission fluxes from 12 μm to 160 μm. Two rectangles are used to subtract the local background. Because W49B shows strong spectral lines (see Figure 5) which contribute important emissions to the middle infrared images, we correct the line contributions by convolving the IRS spectrum with the response curves of *Spitzer* and *MSX*. Because the synchrotron flux of W49B at 6 cm is about 38 Jy and the spectral index is about -0.48 (Moffett & Reynolds 1994), the contribution of electron synchrotron emission to the infrared flux is negligible (The contributed fluxes from 160 μm to 12.1 μm are 2.21, 1.49, 0.89, 0.84, 0.70 and 0.64 Jy). The fluxes at each wavelength are listed in Table 2. We fit a two-component modified blackbody to the dust SED. The function is:

$$S_v = \frac{M_h}{D^2} \times \kappa_v \times B(v, T_h) + \frac{M_w}{D^2} \times \kappa_v \times B(v, T_w), \quad (1)$$

where M_h and M_w represent the masses of the hot and warm dust, $B(v,T)$ is the Plank function and κ_v is the dust absorption cross section per unit mass which is from Draine (2003) with $R_v = 3.1$. Figure 7 displays the result. The hot dust has a temperature of 151 $\pm$ 20 K with mass of 7.5 $\pm$ 6.6 $\times$ 10^{-4} $M_\odot$ and the warm dust has a temperature of 45 $\pm$ 4 K with mass of 6.4 $\pm$ 3.2 $M_\odot$. The dust mass of W49B is calculated using a distance of 10 kpc (see the discussion section for distance).

TABLE 2
FLUXES OF EACH WAVELENGTH USED FOR SED FITTING

Wavelength (μm)	12.1	14.7	21.3	24.0	70.0	160.0
Flux (Jy)	10.80	17.30	49.29	74.06	915.64	418.25
Error (Jy)	2.73	2.89	9.50	9.80	183.13	292.78

4. DISCUSSIONS

4.1. *The distance of W49B*

Previous HI absorption studies suggested W49B at a distance of ~8.0 kpc (Moffett & Reynolds 1994) or ~11.4 kpc (Brogan & Troland 2001). The distance of 8.0 kpc is based on two reasons. The first one is that HI absorptions are seen clearly up to velocity of ~70 km s^{-1} which argues W49B lies behind the tangent point at ~6.2 kpc (assuming Galactic center distance $R_\odot$ = 8.5 kpc and rotation velocity $V_\odot$ = 220 km s^{-1}). The second one is that, compared with W49A, W49B is absent HI absorptions at velocities from 7 to 14 km s^{-1} and 50 to 55 km s^{-1}. The lack of absorption at ~55 km s^{-1} favors W49B is at the distance of ~8.0 kpc. We contrast the HI optical depth (τ_{HI}) of W49B with W49A in Figure 8. The τ_{HI} differences at velocities from 7 to 14 km s^{-1} and 50 to 55 km s^{-1} are confirmed. Beside them, there are other two τ_{HI} differences at velocities of ~40 km s^{-1} (Figure 8a) and ~65 km s^{-1} (Figure 8b) which have similar intensity as the $\Delta\tau_{HI}$ at ~55 km s^{-1}. The HI absorption of different regions of W49B has obvious difference at ~65 km s^{-1} (Figure 8c). Moreover, in the N_{HI}/T_s image toward both W49A and W49B, Brogan & Troland (2001) found there is obvious change on size scales of about 1′. Therefore, the reason supporting the distance of ~8.0 kpc for W49B is not sufficient.

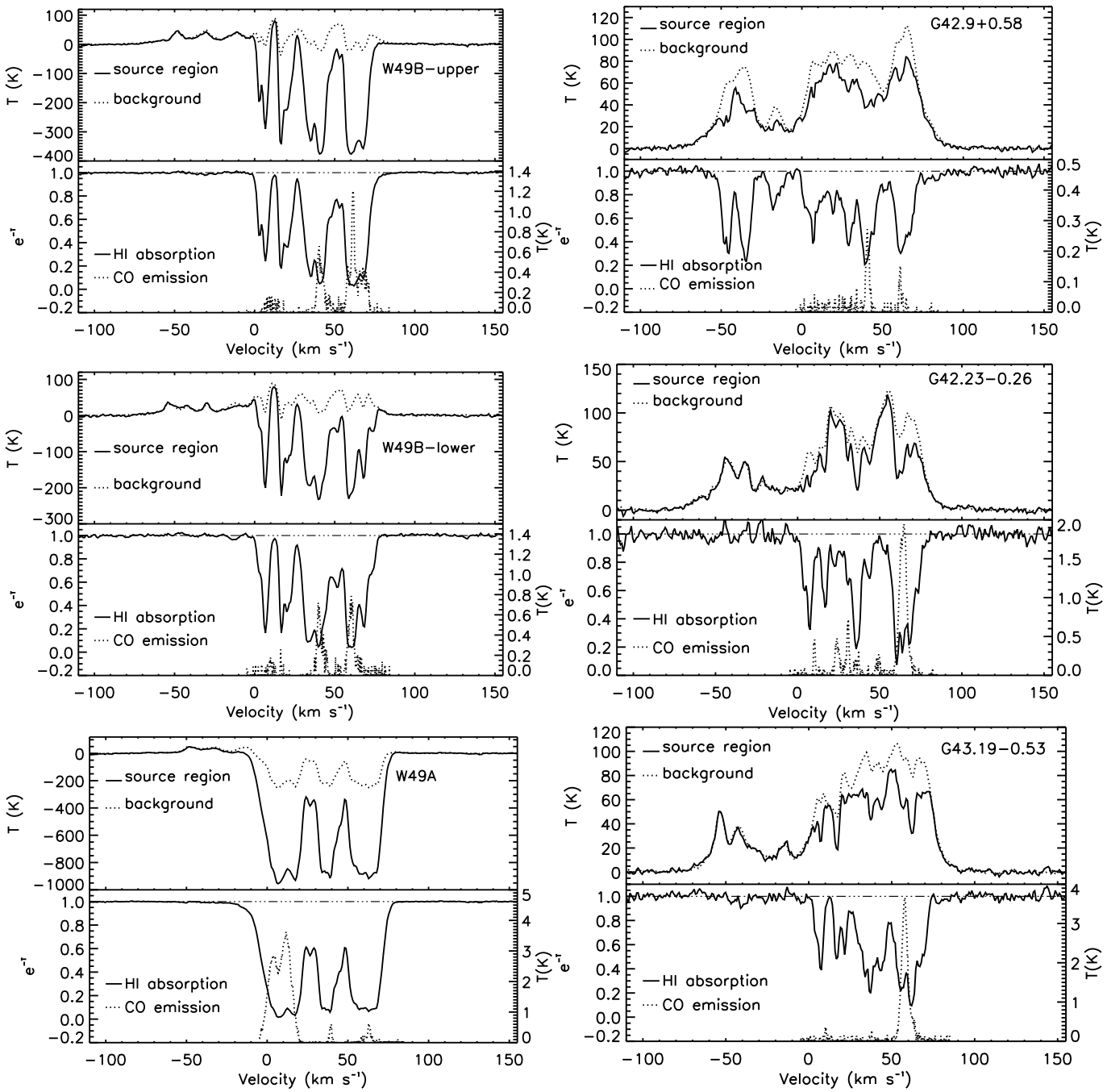

FIG. 2.— HI absorption spectra of W49B, W49A and three nearby HII regions, G42.9+0.58, G42.43-0.26 and G43.19-0.53. In the lower part of each panel, the left Y axis means HI optical depth in the form of $e^{-\tau}$ and the right Y axis represents the brightness temperature of ^{13}CO.

The evidence for distance of 11.4 kpc is weak. Figure 9e of Brogan & Troland (2001) shows the N_{HI}/T_s image of W49B integrated velocities from -4.8 to 12.6 km s^{-1}. They found distinct HI enhancement concentrated toward the south boundary of the SNR. Because the enhancement is coincident with the sharp edge in the 20 cm continuum image, they explained it as the result of interaction between W49B and its ambient medium. If it was true, W49B would locate at the far side distance of $\sim$5 km s^{-1}, i.e. $\sim$12 kpc which is nearly the same distance as W49A. For the HI absorption differences at velocities from 7 to 14 km s^{-1} between W49A and W49B, they suggested it might be caused by the differences of HI kinematics, distribution and temperature in the direction of W49B and W49A. But as illustrated in section 3.1, even with large scale variations of spin temperature, HI absorption at velocity of $\sim$12 km s^{-1} should be visible if W49B is at 11.4 kpc. There are other evidences supporting that W49B is closer than W49A. Figure 9 shows the 2.12 μm image which traces the shocked H_2. The left panels of Figure 10 present the intensity maps of ^{13}CO($J = 1 - 0$) and CO($J = 3 - 2$) integrated from velocity of 1 - 15 km s^{-1}. The shocked H_2 can be seen clearly at the east, south

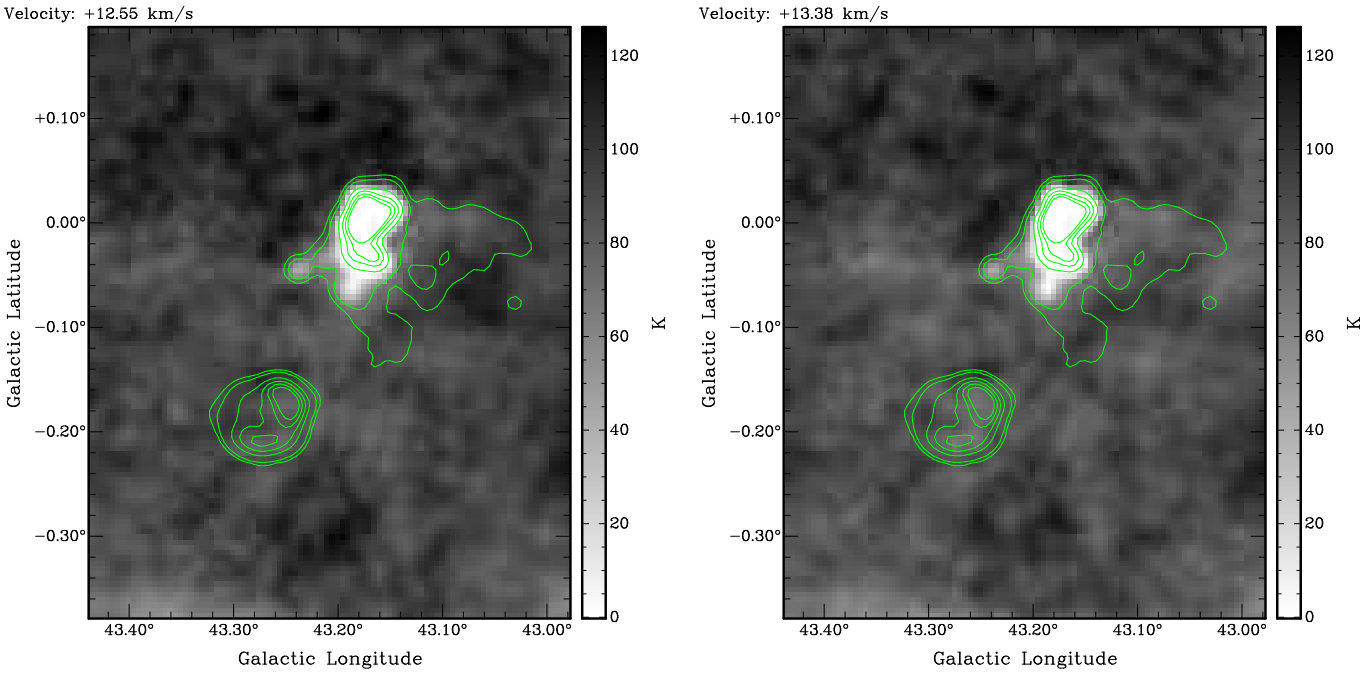

FIG. 3.— HI channel maps at velocities of 12.55 km s^{-1} (Left) and 13.38 km s^{-1} (Right) with the contour same as Figure 1.

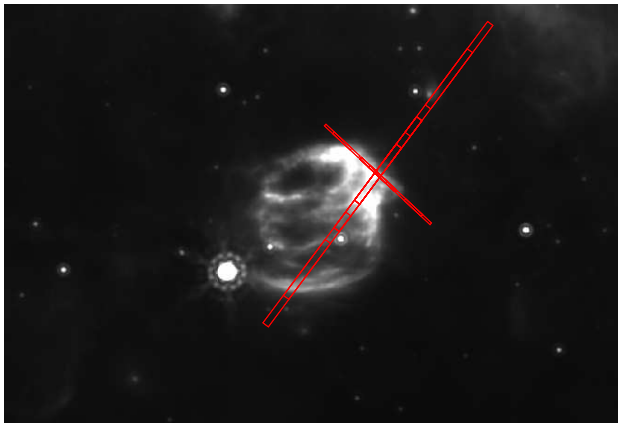

FIG. 4.— *Spitzer* 24 μm image of W49B in Galactic coordinate. Narrow rectangles represent the SL slits and broad rectangles are the LL slits.

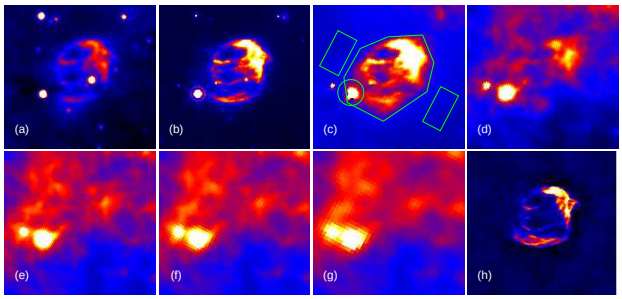

FIG. 6.— Infrared and radio images of W49B in Galactic coordinate. (a): 12 μm from *WISE*; (b): 24 μm from *Spitzer*; (c)-(g): 70 μm, 160 μm, 250 μm, 350 μm, 500 μm from *Herschel*; (h): 20 cm from MAGPIS. The region within the polygon but outside the circle is used to extract the total flux. The two rectangles are used to subtract the local background.

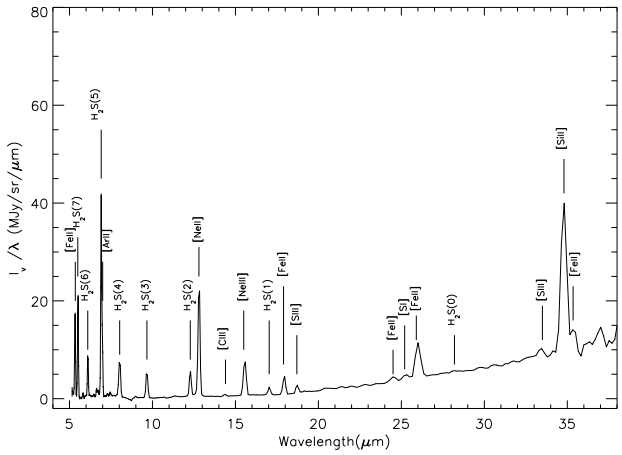

FIG. 5.— IRS spectrum of W49B.

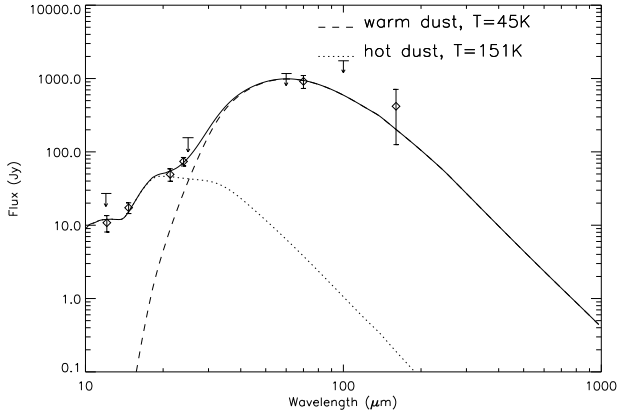

FIG. 7.— Mid- and far-infrared SED of W49B. The dotted line is for the hot component. The dashed line is for the warm component. The solid line is the sum of two components. The upper limits at 12, 25, 60 and 100 μm are from the Improved Reprocessing of the IRAS Survey (Miville-Deschênes & Lagache 2005).

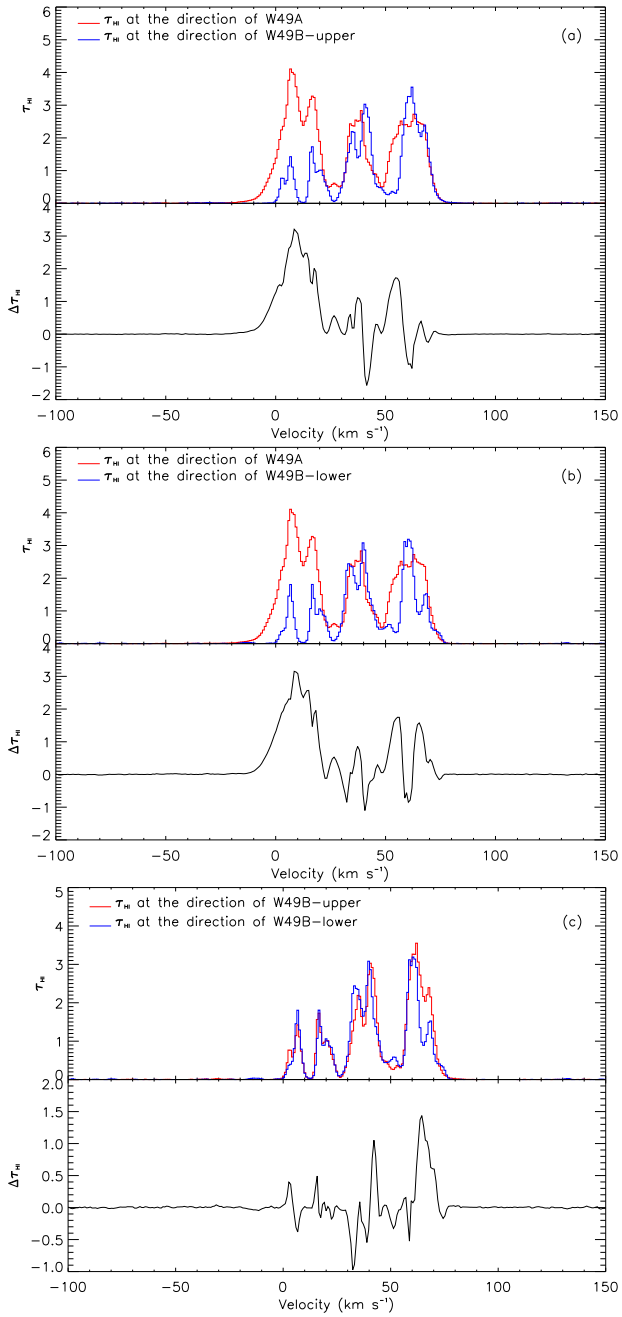

FIG. 8.— HI optical depth towards W49B and W49A.

and west boundaries of W49B, indicating molecular clouds surround W49B except the northern part. This picture is also consistent with the radio continuum image (Figure 4 of Moffett & Reynolds 1994, Figure 2 of Lacey et al. 2001) which shows sharp boundary at the east, south and west and diffuse emission at the north. Diffuse emission means long electron free path length so low medium density. On the contrary, CO clouds at ∼10 km s^{-1} only show strong emission at north. W49B is likely not associated with the 10 km s^{-1} CO clouds so is not at the same distance of W49A.

Since the [Fe II] 1.64 μm, the H_2 2.12 μm morphology and the estimated mass of the progenitor prefer W49B is likely in a bubble surrounded by molecular clouds, we

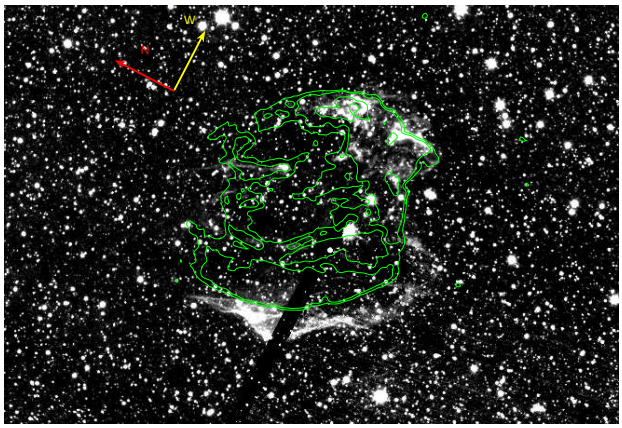

FIG. 9.— 2.12 μm image of W49B in Galactic coordinate. The contours is from 20 cm image of MAGPIS with levels of 3.5, 10, 50 and 100 mJy/beam. The red arrow is for the direction of north and the yellow arrow represents west.

check the distribution of CO emission in the direction of W49B to further constrain its distance. Only the ∼40 km s^{-1} CO cloud has a bubble-like feature (also see Figure 1 of Chen et al. 2014). Because HI self-absorption is detected at velocity of 40 km s^{-1} (Simon et al. 2001), previous study suggested the CO clouds at the near side distance of 40 km s^{-1}. However, we find multi-velocity components in the 40 km s^{-1} CO cloud. We suggest that the 40 km s^{-1} CO cloud is composed of two components: the near side cloud and far side cloud, which also causes additional HI self-absorption. W49B is likely surrounded by the far side CO cloud so has a distance of ∼10 kpc which is similar to Chen et al. (2014)'s suggestion (9.3kpc).

4.2. *The property of the environment of W49B*

4.2.1. *Molecular phase*

Since H_2 (0,0) S(0)-S(7) lines are usually optically thin, the lines' intensity can be used directly to derive the column density of the upper state of the transitions. Therefore the lines are a useful tool to estimate the temperature of the shocked H_2 (Hewitt et al. 2009). Figure 11 is the Boltzmann diagram of the shocked H_2. A striking zig-zag pattern is presented in the figure. This implies that the ortho- to para-state ratio (OPR) of the H_2 is out of equilibrium. Under the local thermodynamic equilibrium, a two temperature distributions model including parameters, $N(H_2)_{w,h}$ (the column density of warm and hot H_2 components), $T_{w,h}$ (the temperature) and $OPR_{w,h}$ (the ortho- to para-state ratio), is used to fit the data. Since a free fitting will make the OPR_w become unreasonable small (less than 10^{-38}), we fix it to be 0.01, 0.05 and 0.10. This leads to a slightly bigger χ^2 than the free fitting. Our result is presented in Figure 11 and Table 3. The three fitting lines almost overlap each other completely, indicating they have similar χ^2. According to the work of Timmermann (1998), the conversion of ortho- to para-state in the shock begins at about 700 K and quickly reachs balance with the ratio of 3 with a temperature of 1300 K. The temperature of the hot H_2 is ∼1060 K with the ortho- to para-state ratio of ∼0.96, this might mean the hot component is going through

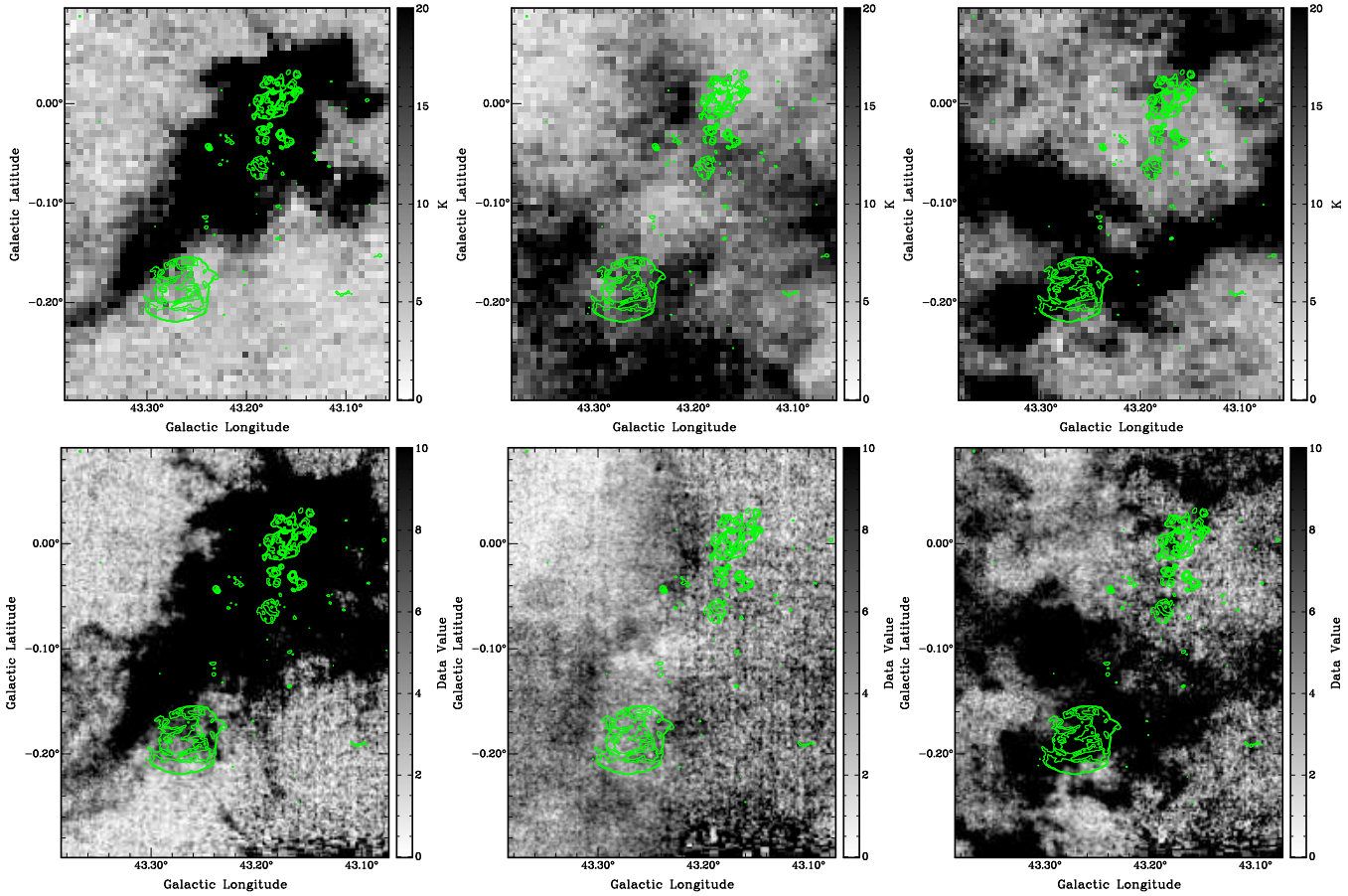

FIG. 10.— Upper: ^{13}CO J=1-0 intensity maps integrated from 1-15 km s^{-1}, 38-47 km s^{-1} and 57-67 km s^{-1}. Lower: CO J=3-2 intensity maps integrated from the same velocity range as ^{13}CO J=1-0 map. The contours in each panel have the same levels as the contour in Figure 9.

TABLE 3
FITTED EXCITATION PARAMETERS TO THE SHOCKED H_2 LINES

Parameter	$N(H_2)_w$ cm^{-2}	T_w K	$N(H_2)_h$ cm^{-2}	T_h K	OPR_h	χ^2
$OPR_w = 0.01$	8.86E20	246	1.38E20	1050	0.97	14.15
$OPR_w = 0.05$	8.41E20	254	1.32E20	1063	0.96	14.56
$OPR_w = 0.10$	6.91E20	266	1.27E20	1075	0.95	15.60

the transition from ortho to para.

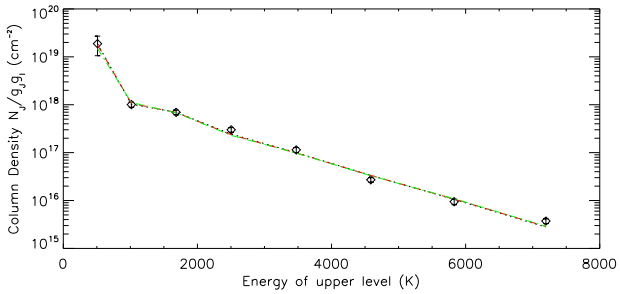

FIG. 11.— Boltzmann diagram of the shocked H_2. The black dotted line represents $OPR_w = 0.01$. The red dashed line is for $OPR_w = 0.05$ and the green dash-dotted line is for $OPR_w = 0.1$.

4.2.2. *Ionic phase*

The abundant ionic spectral lines, especially the Fe^+ and S^{2+} lines, are perfectly diagnostic tools to ionic gas. The [S III] 18.7 μm and 33.48 μm lines are produced by the fine-structure transition of $^3P_2$ to $^3P_1$ and $^3P_1$ to $^3P_0$. As showed in the left panel of Figure 12, since their upper levels have similar temperature, the line intensity ratio is only sensitive to electron density. The right panel of Figure 12 shows the density dependence on the ratio, computed by solving the rate equations for three level systems. Transition probabilities and collision strengths are from Mendoza & Zeippen (1982) and Galavis, Mendoza, & Zeippen (1995) respectively. The collisional deexcitation coefficient is calculated by equation(Osterbrock & Ferland 2006):

$$q_{21} = \int_0^\infty u\sigma_{21} f(u) du = \frac{8.629 \times 10^{-6}}{T^{1/2}} \frac{\Upsilon(1,2)}{g_2}, \qquad (2)$$

where u is the electron velocity, σ_{21} represents the cross section of dedexciation, $f(u)$ is the electron velocity distribution function, $\Upsilon(1,2)$ is the collision strength and g_2 represents statistical weight of the upper level. The collisional excitation coefficient is derived by:

$$q_{12} = \frac{g_2}{g_1} e^{(h\nu_{21}/kT)}. \qquad (3)$$

The red line in the right panel of Figure 12 shows the ratio which indicates an electron density of 500-700 cm^{-3}. Diagnostics of the [Fe II] lines are presented following the work of Hewitt et al. (2009) which use the excitation rate equations of Rho et al. (2001). The line ratio of 17.9/5.35 μm is sensitive primarily to electron density and the ratio of 17.9/25.9 μm depends on both density and temperature. More details can be found in Hewitt et al. (2009). For W49B, the former ratio is 0.25 and the latter value is 0.51. The values prefer a density of 400-600 cm^{-3} and a temperature of $\sim 10^4$ K.

We notice that Keohane et al. (2007) suggested the electron temperature and electron density surrounding W49B are range from (1000 K, 8000 cm^{-3}) to (700 K, 1600 cm^{-3}), which are different from ours. The difference may be caused by two factors. The first one is that Keohane et al. (2007) gave the parameters only using single spectral line (i.e. [Fe II] 1.64 μm) measurement based on some assumptions by considering a wide range of reasonable excitation conditions, but still not covering all possible conditions for SNR (see table 5, 9 of Hewitt et al. 2009 and table 3 of Neufeld et al. 2007), this might cause large uncertainty for the parameters comparing with ours based on a pair of spectral lines which are powerful diagnostic tools for the measurement. The second one is that we might observe parts of W49B different from theirs. As revealed by the *Spitzer* IRS spectrum, W49B has a very complex environment including all three phases gas (the molecular, neutral and ionic gas). In large scale, the temperature and density distribution may form a gradient descent from inner to outside due to the stellar wind before supernova explosion and the interaction between the SNR and its surrounding cloud. If the IRS observation point is closer to inner part compared with Keohane et al. (2007)'s, the electron temperature and density should be higher and more tenuous.

To clarify this explanation, we need compare the spatial distribution of [S III] 18.7 μm and 33.48 μm emission, [Fe II] 5.34 μm, 17.9 μm and 25.9 μm emission with [Fe II] 1.64 μm emission. However only IRS staring mode is used to observe W49B, the comparison will be possible till new data are obtained from IRS mapping mode observation. In addition, our electron temperature and density estimate for W49B are similar with SNR G349.7+0.2 (7000K and 700 cm^{-3}, table 9 of Hewitt et al. 2009). The molecular temperature estimation is also typical (1000-2000 K for hot component, table 3 of Neufeld et al. 2007, table 5 of Hewitt et al. 2009).

Hollenbach & McKee (1989) calculated the low excitation lines' intensity in a J-shock with per-shock medium density of 10^{3-6} cm^{-3}. For W49B, we find a shock with velocity from 60 to 100 km s^{-1} in 10^{3-4} cm $^{-3}$medium can reproduce the main feature of the measured ionic lines. The [Ne III] to [Ne II] line ratio is another indicator of J-shock velocity (Andersen et al. 2011, Hewitt et al. 2009). In Figure 13, we shows the ratio in the W49B based on the model (Hartigan, Raymond, & Hartmann 1987), so we suggest a shock velocity of $\sim$90 km s^{-1}.

4.3. *The dust*

4.3.1. *A comparison with previous result*

The dust property of W49B has been studied by Saken, Fesen, & Shull (1992) (using *IRAS* data) and Pinheiro Gonçalves et al. (2011) (using *Spitzer* data). We find obvious discrepancies between the previous results and ours. The inconsistency is likely caused by the low resolution of *IRAS* data, the neglected spectral line contribution to the total flux in previous study, and different wavelength coverage between the previous and ours.

Using *IRAS* data, Saken, Fesen, & Shull (1992) found W49B has two dust components with temperatures of 157, 35.6 K and dust masses of 0.037 $M_\odot$, 500 $M_\odot$ respectively. However, two factors may lead to wrong result when dealing with *IRAS* data. The first one is related with *IRAS*'s low spacial resolution. As seen in Figure 4, young stellar object G43.31-0.21 (in the circle) with strong infrared emission is nearby W49B. It is impossible to separate them due to *IRAS* low spatial resolution, so the measured flux was the sum of W49B and G43.31-0.21. The second one is that Saken, Fesen, & Shull (1992) did not consider the contribution of various spectral lines to the total flux, especially in the mid-infrared, i.e. the 12 μm band of *IRAS*. Without the correction for the spectral line contribution, the mass of the hot component was overestimated.

Pinheiro Gonçalves et al. (2011) estimated the dust temperature and mass of W49B are 54 K and 1.6 $M_\odot$ using *Spitzer*'s 24 and 70 μm data. The weaknesses are from not considering the spectral line contribution at 24 μm and assuming the flux at 24 μm and 70 μm totally comes from the same dust component. Actually, as displayed in Figure 7, the hot dust contributes the same flux as the warm dust at 24 μm.

Our result also has its weakness. As discussed above, spectral line contribution to the total flux is obvious in the mid-infrared waveband. We try to correct the contribution by the IRS staring mode observation. However, the *Spitzer* IRAC images of W49B (Reach et al. 2006) show different type of line emissions at different position of W49B, e.g. more ionic line emissions in the loops and more molecular line emissions at the east and west part. *Spitzer* IRS observation only covers a small part of W49B which is not enough for detailed line-contribution correction to the remnant.

4.3.2. *The origin of dust*

Supernova (SN) explosion has been considered as the potential source to produce large amounts of dust in a short timescale, i.e. a few Myr. 2-4 $M_\odot$ newly formed cold dust has been detected in the young Galactic SNR, Cas A, which has an age of 320 yr (Dunne et al. 2003). For W49B, the observed infrared emission is not all from newly formed dust, because the total mass of the ejecta is only about 6 $M_\odot$

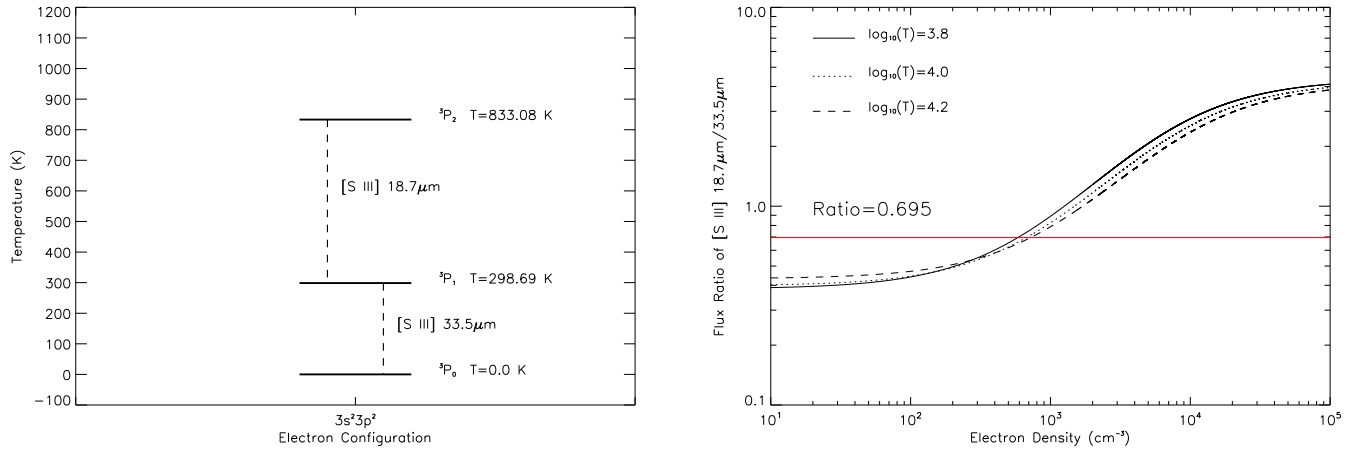

FIG. 12.— Left: Energy levels for [S III] 18.7 μm and 33.5 μm line. Right: Electron density diagnosis from the flux ratio of [S III] 18.7 μm and 33.5 μm line.

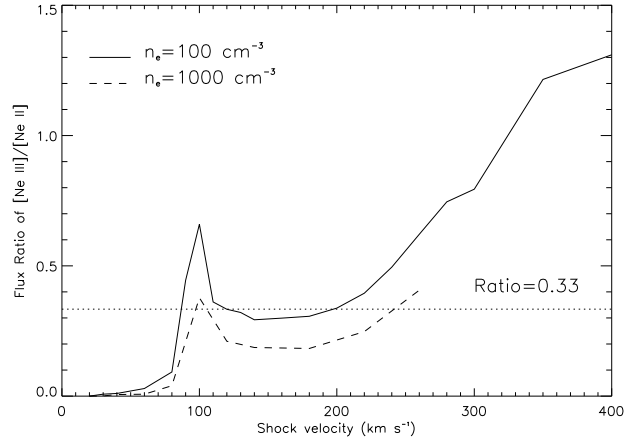

FIG. 13.— Ratio of [Ne III] 15.5 μm and [Ne II] 12.8μm as a function of shock velocity in the shock model of Hartigan et al. (1987). The dotted line represent the ratio.

(Miceli et al. 2008). We have derived that the total mass of dust associated with W49B is 6.4 ± 3.2 $M_\odot$, any newly formed one needs consume all the ejecta to produce dust. Other non-SN origin needs to be explored in order to explain the strong infrared emission of W49B.

W49B's infrared morphology follows the radio emission well, the hot component could be explained naturally by the swept up circumstellar and interstellar material. Assuming a gas to dust ratio of 125 (e.g. Draine 2003), the needed mass of swept up material is a few $\sim 10^{-2} M_\odot$. However, this explanation will not work well for the warm component, because the swept up material will be $\sim$800 $M_\odot$ which is not consistent with the young age of W49B.

Zhou et al. (2011) found the interactions between W49B and the molecular cloud have significant affection on the evolution of the SNR, e.g. the formation of overionized plasma due to the evaporation of the cloud. The work of Inoue et al. (2012) also showed that the densest cloud clumps can survive from the shock and remain inside the SNR. Both works indicate the evaporation of dust from molecular clouds might have a big contribution to the far-infrared emission. Following the work of Lee et al. (2011), the expected infrared emission luminosity of an evaporating cloud in the hot gas of an SNRs can be estimated by equation (Dwek 1981):

$$L_{IR} \approx 200 n_h^2 (\frac{R_c}{1pc})^3 (\frac{T_h}{10^7 K})^{1.5} L_\odot, \quad (4)$$

where R_c is the radius of the cloud, n_h and T_h are the density and temperature of the hot gas. For W49B, n_h is about 5 cm^{-3} (Miceli et al. 2008). T_h is range from 1.13 keV to 3.68 keV or 1.31 $\times 10^7$ K to 4.27 $\times 10^7$ K obtained from X-ray spectral fitting of different regions of W49B and by different authors (Miceli et al. 2006, Keohane et al. 2007, Ozawa et al. 2009, Lopez et al. 2009, Miceli et al. 2010, Lopez et al. 2013a). We also estimated the T_h by an indirect way using equation (McKee & lenbach 1980):

$$T_h = (\frac{v_r}{839 kms^{-1}})^2 \times 10^7 K, \quad (5)$$

where v_r is the forward shock velocity in the plasma. Keohane et al. (2007) estimated the v_r to be $\sim$1200 km s^{-1} for W49B. So the T_h is derived to be $\sim 2.0 \times 10^7$ K which is well consistent with the value from X-ray spectral analysis. If we use the value of 2.0×10^7 K and assume a radius of $2.3^{+0.3}_{-0.5}$ pc for the evaporation cloud, the emission of evaporated dusts will have the same luminosity as the observation, i.e. 17.0 ± 8.5 $\times 10^4 L_\odot$ derived from equation, $L = \int \kappa_v B(v,T) M_{dust} dv$. Higher T_h, such as 2.5×10^7 K or 3.0×10^7 K, will reduce the radius to $2.0^{+0.3}_{-0.4}$ pc or $1.9^{+0.2}_{-0.4}$ pc. W49B has a dense environment, dust from evaporation clouds is feasible way to explain the observed far-infrared emission.

5. SUMMARY

We study W49B and its environment by radio and infrared observations. We detect fluctuation in the absorption spectrum toward different part of W49B and W49A which support Brogan & Troland (2001)'s suggestion that the difference of HI distribution could explain the absorption difference at $\sim$55 km s^{-1} between

W49B and W49A. We conclude that the previous claim of W49B interacting with clouds at the southern boundary at velocity of ∼5 km s^{-1} is likely not right. W49B is instead of likely associated with molecular cloud at ∼40 km s^{-1}, this suggests that W49B has a distance of ∼10 kpc.

Spitzer IRS observation reveals clear pure rotational shocked H_2 lines, H_2 (0,0) S(0)-S(7), which supports W49B is interacting with molecular cloud. Boltzmann diagram suggests there are two components of H_2 with temperatures of ∼260 K and ∼1060 K. Spectral lines of S^0, S^{2+}, Ar^+, Cl^+, Fe^+, Ne^+, Ne^{2+} and Si^+ are also detected. We find the ionic phase has electron density of ∼500 cm^{-3} with a temperature of ∼ 10^4 K. A J-shock with velocity of ∼90 km s^{-1} may produce the main ionic spectral line features.

Mid- and far-infrared SED fitting implies there are two components of dust with temperature of 151 ± 20 K and 45 ± 4 K associated with W49B. Each components have masses of 7.5 ± 6.6 × $10^{-4} M_\odot$ and 6.4 ± 3.2 $M_\odot$ respectively. The hot dust can be explained by the swept up circumstellar or interstellar materials. The warm dust may originate from evaporation of the clouds interacting with W49B.

HZ and WWT acknowledge supports from NSFC (211381001, Y211582001) and BaiRen programme of the CAS (034031001). This work is partly supported by China's Ministry of Science and Technology under State Key Development Program for Basic Research (2012CB821800, 2013CB837901). We thank Drs Y. Zhang, X.L. Liu, P. Wei, X.M. Wang and Y. Su for meaningful discussion when preparing this paper. This research has made use of the NASA/ IPAC Infrared Science Archive, which is operated by the Jet Propulsion Laboratory, California Institute of Technology, under contract with the National Aeronautics and Space Administration.

REFERENCES

Abdo, A. A., Ackermann, M., Ajello, M., et al. 2010, ApJ, 722, 1303
Andersen, M., Rho, J., Reach, W. T., Hewitt, J. W., & Bernard, J. P. 2011, ApJ, 742, 7
Brogan, C. L., & Troland, T. H. 2001, ApJ, 550, 799
Brun, F., de Naurois, M., Hofmann, W., et al. 2011, ArXiv e-prints
Carey, S. J., Noriega-Crespo, A., Mizuno, D. R., et al. 2009, PASP, 121, 76
Chen, Y., Jiang, B., Zhou, P., et al. 2014, in IAU Symposium, Vol. 296, IAU Symposium, ed. A. Ray & R. A. McCray, 170–177
Dempsey, J. T., Thomas, H. S., & Currie, M. J. 2013, ApJS, 209, 8
Draine, B. T. 2003, ARA&A, 41, 241
Dunne, L., Eales, S., Ivison, R., Morgan, H., & Edmunds, M. 2003, Nature, 424, 285
Dwek, E. 1981, ApJ, 246, 430
Froebrich, D., Davis, C. J., Ioannidis, G., et al. 2011, MNRAS, 413, 480
Fujimoto, R., Tanaka, Y., Inoue, H., et al. 1995, PASJ, 47, L31
Galavis, M. E., Mendoza, C., & Zeippen, C. J. 1995, A&AS, 111, 347
Griffin, M., Ade, P., André, P., et al. 2009, in EAS Publications Series, Vol. 34, EAS Publications Series, ed. L. Pagani & M. Gerin, 33–42
Gwinn, C. R., Moran, J. M., & Reid, M. J. 1992, ApJ, 393, 149
Hartigan, P., Raymond, J., & Hartmann, L. 1987, ApJ, 316, 323
Helfand, D. J., Becker, R. H., White, R. L., Fallon, A., & Tuttle, S. 2006, AJ, 131, 2525
Hewitt, J. W., Rho, J., Andersen, M., & Reach, W. T. 2009, ApJ, 694, 1266
Hollenbach, D., & McKee, C. F. 1989, ApJ, 342, 306
Houck, J. R., Roellig, T. L., van Cleve, J., et al. 2004, ApJS, 154, 18
Hwang, U., Petre, R., & Hughes, J. P. 2000, ApJ, 532, 970
Inoue, T., Yamazaki, R., Inutsuka, S.-i., & Fukui, Y. 2012, ApJ, 744, 71
Jackson, J. M., Rathborne, J. M., Shah, R. Y., et al. 2006, ApJS, 163, 145
Keohane, J. W., Reach, W. T., Rho, J., & Jarrett, T. H. 2007, ApJ, 654, 938
Lacey, C. K., Lazio, T. J. W., Kassim, N. E., et al. 2001, ApJ, 559, 954
Lee, H.-G., Moon, D.-S., Koo, B.-C., et al. 2011, ApJ, 740, 31
Lockhart, I. A., & Goss, W. M. 1978, A&A, 67, 355
Lockman, F. J. 1989, ApJS, 71, 469
Lopez, L. A., Pearson, S., Ramirez-Ruiz, E., et al. 2013a, ApJ, 777, 145
Lopez, L. A., Ramirez-Ruiz, E., Castro, D., & Pearson, S. 2013b, ApJ, 764, 50
Lopez, L. A., Ramirez-Ruiz, E., Pooley, D. A., & Jeltema, T. E. 2009, ApJ, 691, 875
Mandelartz, M., & Becker Tjus, J. 2013, ArXiv e-prints
McKee, C. F., & lenbach, D. J. 1980, ARA&A, 18, 219
Mendoza, C., & Zeippen, C. J. 1982, MNRAS, 199, 1025
Miceli, M., Bocchino, F., Decourchelle, A., Ballet, J., & Reale, F. 2010, A&A, 514, L2
Miceli, M., Decourchelle, A., Ballet, J., et al. 2008, Advances in Space Research, 41, 390
—. 2006, A&A, 453, 567
Miville-Deschênes, M.-A., & Lagache, G. 2005, ApJS, 157, 302
Moffett, D. A., & Reynolds, S. P. 1994, ApJ, 437, 705
Neufeld, D. A., Hollenbach, D. J., Kaufman, M. J., et al. 2007, ApJ, 664, 890
Osterbrock, D. E., & Ferland, G. J. 2006, Astrophysics of gaseous nebulae and active galactic nuclei, 2nd. ed., Unicersity Science Book, Sausalito
Ozawa, M., Koyama, K., Yamaguchi, H., Masai, K., & Tamagawa, T. 2009, ApJ, 706, L71
Pinheiro Gonçalves, D., Noriega-Crespo, A., Paladini, R., Martin, P. G., & Carey, S. J. 2011, AJ, 142, 47
Poglitsch, A., Waelkens, C., Geis, N., et al. 2010, A&A, 518, L2
Price, S. D., Egan, M. P., Carey, S. J., Mizuno, D. R., & Kuchar, T. A. 2001, AJ, 121, 2819
Pye, J. P., Becker, R. H., Seward, F. D., & Thomas, N. 1984, MNRAS, 207, 649
Radhakrishnan, V., Goss, W. M., Murray, J. D., & Brooks, J. W. 1972, ApJS, 24, 49
Reach, W. T., Rho, J., Tappe, A., et al. 2006, AJ, 131, 1479
Rho, J., Jarrett, T. H., Cutri, R. M., & Reach, W. T. 2001, ApJ, 547, 885
Saken, J. M., Fesen, R. A., & Shull, J. M. 1992, ApJS, 81, 715
Simon, R., Jackson, J. M., Clemens, D. P., Bania, T. M., & Heyer, M. H. 2001, ApJ, 551, 747
Smith, A., Peacock, A., Jones, L. R., & Pye, J. P. 1985, ApJ, 296, 469
Stil, J. M., Taylor, A. R., Dickey, J. M., et al. 2006, AJ, 132, 1158
Tian, W. W., & Leahy, D. A. 2008, ApJ, 677, 292
Tian, W. W., Leahy, D. A., & Wang, Q. D. 2007, A&A, 474, 541
Timmermann, R. 1998, ApJ, 498, 246
Traficante, A., Calzoletti, L., Veneziani, M., et al. 2011, MNRAS, 416, 2932
Wood, D. O. S., & Churchwell, E. 1989, ApJS, 69, 831
Wright, E. L., Eisenhardt, P. R. M., Mainzer, A. K., et al. 2010, AJ, 140, 1868
Yang, X. J., Tsunemi, H., Lu, F. J., et al. 2013, ApJ, 766, 44
Zhou, X., Miceli, M., Bocchino, F., Orlando, S., & Chen, Y. 2011, MNRAS, 415, 244